Using Image Processing Techniques to Identify and Quantify Spatiotemporal Carbon Cycle Extremes

1st Bharat Sharma
Computational Earth Sciences Group
Oak Ridge National Laboratory
Oak Ridge, USA
bharat.sharma.neu@gmail.com

Department of Civil and Environmental Engineering
Northeastern University
Boston, USA
orcid.org/0000-0002-6698-2487

2nd Jitendra Kumar
Environmental Sciences Division
Oak Ridge National Laboratory
Oak Ridge, USA
orcid.org/0000-0002-0159-0546

3rd Auroop R. Ganguly
Department of Civil and Environmental Engineering
Northeastern University
Boston, USA
orcid.org/0000-0002-4292-4856

4th Forrest M. Hoffman
Computational Earth Sciences Group
Oak Ridge National Laboratory
Oak Ridge, USA
orcid.org/0000-0001-5802-4134

Abstract—Rising atmospheric carbon dioxide due to human activities through fossil fuel emissions and land use changes have increased climate extremes such as heat waves and droughts that have led to and are expected to increase the occurrence of carbon cycle extremes. Carbon cycle extremes represent large anomalies in the carbon cycle that are associated with gains or losses in carbon uptake. Carbon cycle extremes could be continuous in space and time and cross political boundaries. Here, we present a methodology to identify large spatiotemporal extremes (STEs) in the terrestrial carbon cycle using image processing tools for feature detection. We characterized the STE events based on neighborhood structures that are three-dimensional adjacency matrices for the detection of spatiotemporal manifolds of carbon cycle extremes. We found that the area affected and carbon loss during negative carbon cycle extremes were consistent with continuous neighborhood structures. In the gross primary production data we used, 100 carbon cycle STEs accounted for more than 75% of all the negative carbon cycle extremes. This paper presents a comparative analysis of the magnitude of carbon cycle STEs and attribution of those STEs to climate drivers as a function of neighborhood structures for two observational datasets and an Earth system model simulation.

Index Terms—carbon cycle extremes, spatiotemporal extremes, attribution analysis, climate drivers, scale-free networks

I. INTRODUCTION

Increased production and use of fossil fuels and deforestation have led to an increase in the atmospheric concentration of greenhouse gases (GHGs), most importantly carbon dioxide (CO_2), methane, and nitrous oxide. The increased concentration of GHGs is driving a rise in the surface temperature of the Earth, amplifying climate variability, and increasing the occurrence of climate extremes [1]. Terrestrial ecosystems have historically taken up about 30% of anthropogenic CO_2 emissions via carbon accumulation in plant biomass and soils [2]. The increased carbon fertilization and water use efficiency, and the lengthening of growing seasons are increasing terrestrial carbon uptake and limiting the rise in atmospheric concentration of CO_2 [3]. However, exacerbating climate extremes over time—such as droughts, heat waves, and fires—have the potential to reduce terrestrial carbon uptake [1], [4]–[6].

Recent studies have focused on detecting and quantifying extremes in the impacted systems, such as carbon cycle extremes [7]–[9], and attribution of those extremes to climate drivers. Recent studies have analyzed spatiotemporal continuous extremes in the carbon cycle using $3\times3\times3$ voxels and found that a few of these continuous extremes represent most

of the interannual variability in the terrestrial carbon cycle [10], [11]. However, whether extreme events in the carbon cycle are discrete or continuous is an open question. While the answer to this question is beyond the scope of this paper, we analyzed the proximity of carbon cycle extremes to each other, in the spatiotemporal manifold of connected grid cells, depending on the shape of a three dimensional search cube or voxel. This is the first study that has quantified and compared the characteristics of continuous and non-continuous extremes in the global carbon cycle.

We defined six unit neighborhood structures composed of isolated or non-continuous extremes that are (1) continuous only in time, (2) continuous only in space, or (3) continuous in both space and time (Figure 1). We analyzed and compared the characteristics of non-continuous, constrained continuous, and continuous extremes in GPP for observational datasets and Earth system model (ESM) outputs. We then calculated the representative climatic conditions for such carbon cycle extremes to attribute them to climate drivers. We also investigated the characteristics of the connected network of carbon cycle extremes, which indicates how close, in space and time, extremes in terrestrial ecosystems occur. The objectives of this study were to a) use image processing techniques to detect spatiotemporal manifolds of extreme events in GPP, referred to in this paper as spatiotemporal extremes (STEs), b) compare the characteristics of STEs identified in ESM simulation output with those from gridded observational datasets, and c) attribute the STEs in GPP to climate drivers.

II. DATA

We used two observation-based, up-scaled GPP data products, FluxANN and GOSIF, and Earth system model output from the Community Earth System Model version 2 (CESM2) from an historical simulation conducted for the sixth phase of the Coupled Model Intercomparison Project (CMIP6). FLUXCOM provides global gridded carbon fluxes from two experimental setups, one with only remote sensing ("RS") input drivers and the other with RS and meteorological drivers ("RS+METEO"). The FluxANN dataset is "FLUXCOM RS+METEO", which used CRUN-CEPv6 climate reanalysis and an Artificial Neural Network (ANN) [12]. FluxANN was produced at $0.5° \times 0.5°$ spatial and monthly temporal resolution, and it is available at https://www.fluxcom.org/. The GOSIF dataset was produced using global Solar-induced chlorophyll fluorescence (SIF) from discrete Orbiting Carbon Observatory-2 (OCO-2) SIF soundings, remote sensing data from MODIS, and meteorological reanalysis data [13]. GOSIF was produced at $0.05° \times 0.05°$ spatial and 8-day temporal resolution, and it is accessible at https://globalecology.unh.edu/data/GOSIF-GPP.html. For attribution of GPP STEs from observations, we used climate driver data from the fifth generation European Centre for Medium-Range Weather Forecasts (ECMWF) reanalysis (ERA5) product. ERA5 is produced at $0.1° \times 0.1°$ spatial and hourly temporal resolution, and it is accessible at https://www.ecmwf.int/en/forecasts/datasets/reanalysis-datasets/era5.

The CESM2 simulation was performed at $0.9375° \times 1.25°$ spatial resolution, and monthly output was used here. CESM2 is a fully coupled global Earth system model composed of atmosphere, ocean, land, sea ice, and land ice components. The CESM2 simulation output can be downloaded from https://www.cesm.ucar.edu/models/cesm2/.

III. METHODS

A. *Data Preprocessing*

The spatial resolutions of observation based GPP-datasets are $0.5°$ and $0.05°$ for FluxANN and GOSIF, respectively, and $0.1°$ for the ERA5 climate data. For consistent comparison of extremes and attribution, GOSIF and ERA5 were conservatively regridded to $0.5°$ spatial resolution using TempestRemap [14], [15]. Both observational datasets were aggregated to monthly average timeseries. A common time period from 2001-01-01 to 2013-12-31 (156 months) was chosen and all datasets were trimmed to this study period.

We used the GPP datasets from up-scaled observational data products (FluxANN and GOSIF) and from CESM2 to quantify spatiotemporal extreme (STE) events in GPP, also referred to as carbon cycle STEs, in this paper. These carbon cycle STEs represented anomalous gains or losses in GPP or total photosynthetic uptake. Recent studies [8], [9] have found that the magnitude and frequency of negative carbon cycle extremes is expected to be larger than that of positive extremes. Hence, we focused our analysis on the detection and attribution of negative carbon cycle STEs, which potentially have larger impacts on the carbon cycle than positive extremes. For attribution of negative STEs in the carbon cycle to climatic conditions, we chose surface air temperature (*tas*) and precipitation (*pr*) datasets.

Most variables in the Earth system have some possibly nonlinear trend and a modulated annual cycle. We defined the nonlinear trend as signals in the time series that are comprised of return periods of 10 years and longer [9]. The modulated annual cycle is composed of signals with return periods of 12 months and its harmonics. To extract the nonlinear trend and modulated annual cycle from each variable, we used singular spectral analysis [9], [16].

Data preprocessing is an important step that could have varying impact on results, especially because the scope of spatiotemporal carbon cycle extremes in this study was global [11]. We followed the data preprocessing steps as described by Zscheischler et al. [11]. The anomalies in GPP were calculated by subtracting the trend and the annual cycle; thus, the reported losses during negative carbon cycle extremes were absolute global losses in potential carbon uptake, which allows for comparison across time. For compatibility across space, the

trend and annual cycle were subtracted from *tas*, and scaled by dividing by standard deviation at every grid cell. For *pr*, the trend was removed and the detrended *pr* at every grid cell was normalized by dividing with total *pr*.
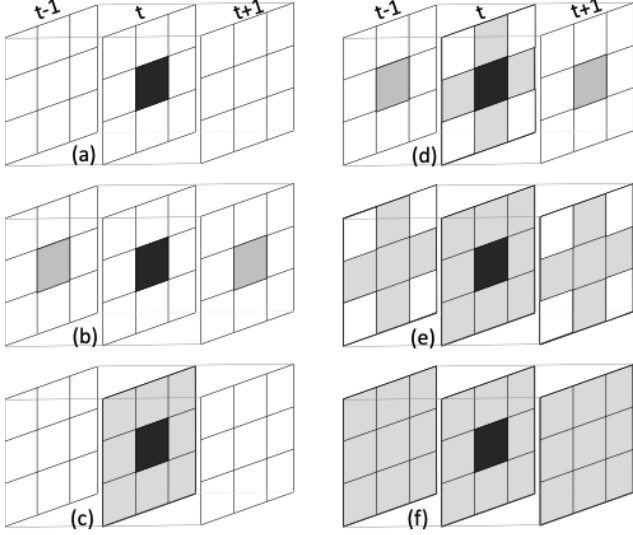
B. *Detection of Carbon Cycle Extremes*

Fig. 1: Different unit neighborhood structures of spatiotemporal extreme (STE) events. a) sesd: small extent short duration; b) seld: small extent long duration; c) lesd: large extent short duration; d) 6-n: 6 neighbors; e) 18-n: 18 neighbors; and f) leld: large extent long duration or 26 neighbors

Based on the global probability distribution of GPP anomalies, we selected the 10th percentile value [17], q_{10}, such that total positive and negative extremes constitute 10% of all GPP anomalies [8]. GPP anomalies less than q_{10} were called negative carbon cycle extremes, and a three-dimensional (3D) mask of GPP extremes was calculated to produce data cubes of 1 and 0 values. A value of 1 and 0 represented occurrence and non-occurrence of negative carbon cycle extremes, respectively. We defined six neighborhood structures as shown in the Figure 1, that were used to search for the connected 3D manifold of carbon cycle extremes. To find connected spatiotemporal extremes (STEs), we used the *ndarray* library in Python. *ndarray* connects the neighborhood structures using the adjacency matrix and assigns unique labels to each manifold.

C. *Attribution of Spatiotemporal Carbon Cycle Extremes*

We quantified the response variable, GPP, within STE manifolds, then we computed the climatic conditions that could have driven such STEs in GPP. We calculated the representative climatic conditions using the median of the climate drivers throughout the spatiotemporal masks of the corresponding

negative STEs in GPP. Since terrestrial vegetation has an innate plastic capacity to buffer the impact of short duration climate extremes [18], we computed the median of the climate drivers ($tas_{STE,t}$, $pr_{STE,t}$) during and up to three months (N) prior to the occurrence of STEs in GPP. We assumed that the *tas* anomalies larger than the 75th percentile represented hot climatic conditions and *pr* anomalies smaller than the 25th percentile represented dry conditions. We performed the attribution analysis on the largest 100 STEs in GPP such that the number of negative carbon cycle STEs driven by dry, wet, $cold$, or hot were computed as shown in equations here,

$$\#dry = pr_{STE,t} < pr_{25q,t} \mid t \in N \qquad (1)$$

$$\#wet = pr_{STE,t} > pr_{75q,t} \mid t \in N \qquad (2)$$

$$\#cold = tas_{STE,t} < tas_{25q,t} \mid t \in N \qquad (3)$$

$$\#hot = tas_{STE,t} > tas_{75q,t} \mid t \in N \qquad (4)$$

where $25q$ and $75q$ indicate the 25th and 75th percentile values of a climate driver at t months prior to the occurrence of STE events. N is the total number of months (here, $N = 3$) considered for lagged response of GPP on the climate drivers.

D. *Scale-Free Property of Carbon Cycle STEs*

In a scale-free network, degree distribution of the nodes of the network follows a power law [22], such that the probability of a randomly chosen node, n, is $p(n)$ and has γ links to other nodes.

$$p(n) = Cn^{-\gamma} \qquad (5)$$

$$p(n) = \log C + -\gamma \log n \qquad (6)$$

Many networks exhibit the scale-free property, such as, the Internet, actor networks, air traffic networks, etc. For example, in an air traffic network, most large airports act as hubs and have a large number of links to other large hubs and small airports [23]. Thus, the degree distribution in a scale-free network has a few nodes with large degree and most nodes with a small degree. This is in contrast to a random network of, say, state highways, in which we have a small number of highways for every city and, hence, the degree distribution per node is similar to the average degree distribution of the entire network. Similar scale-free properties have been observed in the disturbance of extreme events in terrestrial ecosystems as well [11]. Since the STEs in the carbon cycle are a large scale connected component of extremes, we performed the power law fit for STEs in GPP for both FluxANN and CESM2 for multiple neighborhood structures.

(a) Magnitude of Negative Carbon Cycle Extremes from FluxANN (Tg C)

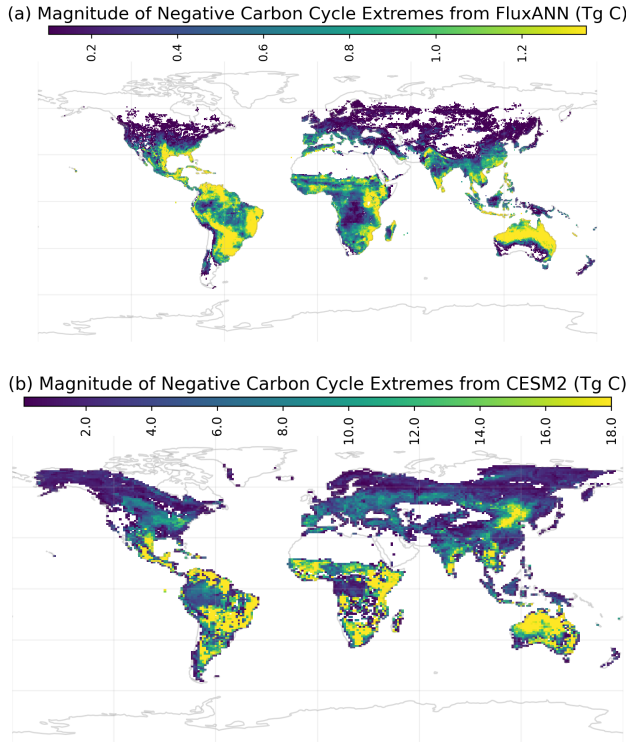(b) Magnitude of Negative Carbon Cycle Extremes from CESM2 (Tg C)

Fig. 2: The figure shows the spatial distribution of the integrated sum of carbon uptake loss (Tg C) during negative carbon cycle extremes for (a) FluxANN and (b) CESM2.

IV. RESULTS AND DISCUSSION

A. *Characteristics of Carbon Cycle STEs*

The annual mean magnitude of total GPP of terrestrial ecosystem was about $115\,\mathrm{Pg\,C\,yr^{-1}}$ for both FluxANN and CESM2 from 2001 to 2013. However, the annual average loss in carbon uptake during negative carbon cycle extremes was $1.6\,\mathrm{Pg\,C\,yr^{-1}}$ for FluxANN and $5.5\,\mathrm{Pg\,C\,yr^{-1}}$ for CESM2. The larger magnitude of negative carbon cycle extremes is largely driven by a larger amplitude of interannual variability (IAV) in the terrestrial carbon cycle [9]. This implies that CESM2 was overestimating the IAV in GPP, FluxANN was underestimating the IAV in GPP, or both. Jung et al. [12] investigated the bias and interannual variability metrics of FLUXCOM and concluded that FLUXCOM and FluxANN have a stronger carbon uptake strength in the tropics due to a positive bias in the underlying eddy covariance data. Moreover, the IAV in GPP was weaker in FLUXCOM than in dynamic global vegetation models. The main reason for the underestimation of IAV in FLUXCOM is due to the sparsity of observational sites, lack of site historical data, and smoothing by machine learning models [12].

The spatial distribution of the magnitude of negative carbon cycle extremes for FluxANN (Figure 2a) and CESM2 (Figure 2b) indicate large agreement on the spatial distribution
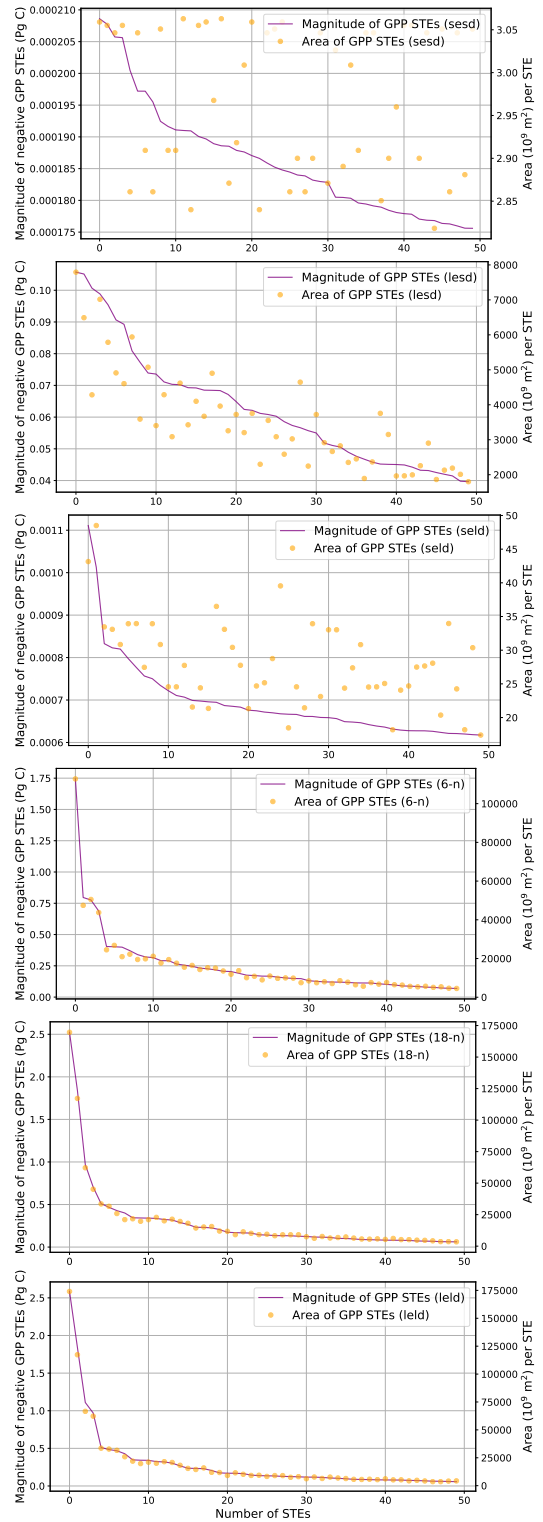

Fig. 3: Plots of the loss of carbon uptake (Pg C) for each negative carbon cycle STE geometry for FluxANN, shown as a line plot (left y-axis). The filled circles represent the corresponding affected area (10^{+9} m^2) for each negative carbon cycle STE geometry (right y-axis). The x-axis represents the top 50 negative carbon cycle STEs in descending order of magnitude.

of negative carbon cycle extremes, but disagreement on the magnitude of those extremes. The regions that show the largest magnitude of negative carbon cycle extremes were the Amazon Basin, Central and Southern South America, Eastern Africa, Eastern China, and Northern Australia. Due to low IAV in GPP in FluxANN [12], the magnitude of negative carbon cycle extremes was smaller compared to the negative carbon cycle extremes simulated by CESM2.

The area affected and magnitude of STEs in GPP increased with the size of the neighborhood structure. Figure 3 shows the distribution of the magnitude of the negative carbon cycle STEs in FluxANN in decreasing order of magnitude and the corresponding area affected during STEs. The largest magnitude of negative carbon cycle extremes with the *sesd* structure was 2×10^{-4} Pg C (Figure 3a), whereas the largest negative STE with *leld* structure was 2.5 Pg C (Figure 3f). With increasing size of neighborhood structure, the area and magnitude of STEs showed a consistent relationship with the distribution of ranked STEs.

Figure 4 shows the cumulative losses in carbon uptake (GPP, Pg C) with increasing number of STEs. The top 10 STEs for *leld* account for about 45%, 65% and 85% of the total loss of carbon uptake for FluxANN, CESM2, and GOSIF, respectively. The top 100 STEs for *leld* account for more than 75% of the total carbon losses, which demonstrates that only a few large STEs can explain most of the variability and losses in GPP. This finding is consistent with the results of [10]. As the neighborhood structure size is reduced, a larger number of STEs are required to account for similar losses in carbon cycle uptake (Figures 4a and 4b).

The total cumulative losses in the observation-based datasets, FluxANN and GOSIF, were about 20.9 Pg C and 73.4 Pg C, respectively. The larger magnitude of negative carbon cycle extremes in GOSIF were due to the larger magnitude and point density of IAV in GPP (Figure 5) with respect to FluxANN. These differences also highlighted large disagreements among different observation-based datasets. The spatial resolution of GOSIF is 10 times finer than FluxANN and likely represents more variance in the carbon cycle; the ANN used to up-scale point observations to a coarser gridded dataset was smoothed and represents lower variance in the carbon cycle [12].

B. *Scale-free Property of STEs*

Figure 6 shows the power law fit for the structure *leld* for both FluxANN and CESM2. The exponent, γ_{leld}, for FluxANN and CESM2 was 1.83 and 1.79, respectively, despite the different spatial resolutions of these datasets. For every neighborhood structure that has continuity in both space and time, i.e., $6-n$, $18-n$, and *leld*, $1.75 < \gamma < 2$ as shown in Table I, which is also consistent with the literature [10], [11].

For a scale-free network, the natural cutoff is represented as [22]

$$n_{max} = n_{min} \; M^{\frac{1}{\gamma-1}} \tag{7}$$
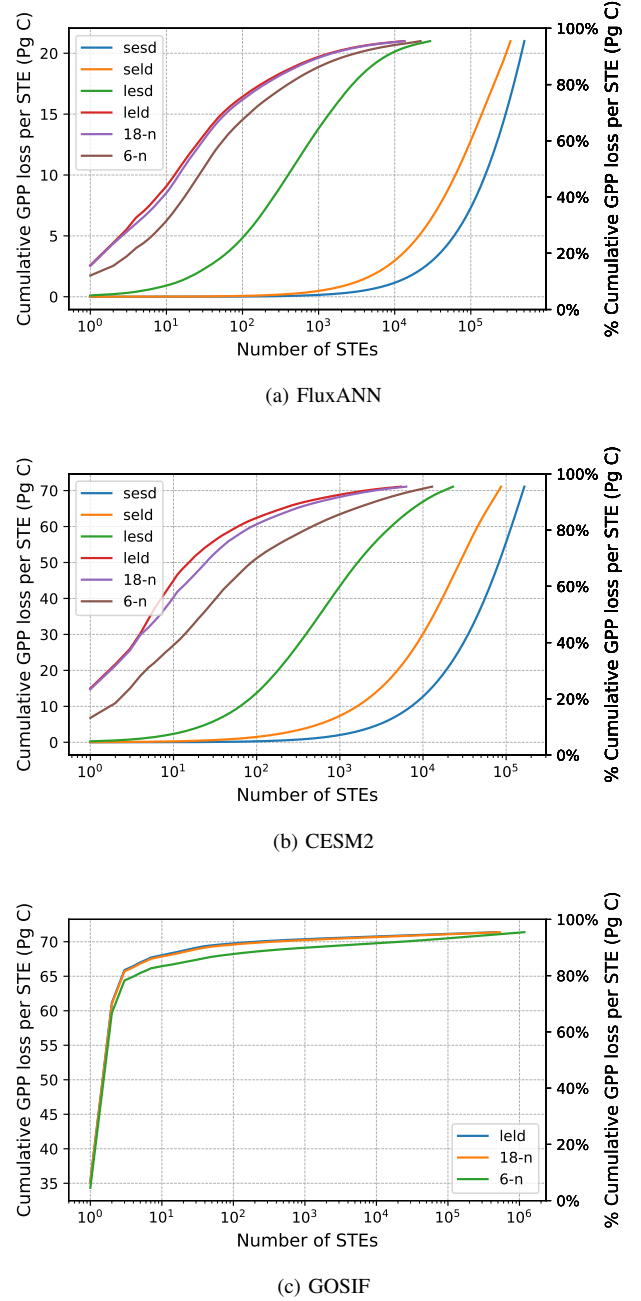

(a) FluxANN

(b) CESM2

(c) GOSIF

Fig. 4: Plot of cumulative loss of carbon uptake during negative carbon cycle STEs. The distribution of magnitude (left y-axis) and percent carbon uptake loss (right y-axis) are shown in descending order of the magnitude of STEs. These distributions are shown for all neighborhood structures for (a) FluxANN and (b) CESM2. For (c) GOSIF, the distribution of GPP loss vs. number of STEs is shown only for *leld*, *18-n*, and *6-n*.
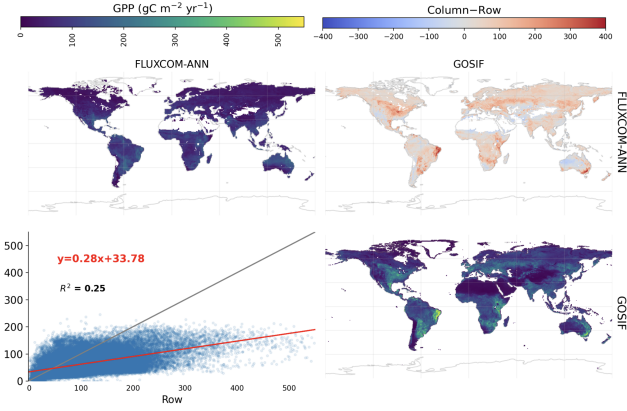
Fig. 5: Left and right, and top and bottom, show the FLUXCOM-ANN (FluxANN) and GOSIF, respectively. The diagonal maps show the IAV of GPP of both datasets. The map above the diagonal shows the difference of the IAV of GPP of column dataset − row dataset. The map below the diagonal shows the point density in blue and 1:1 regression line in grey. Red line and equation represent the best fit line from total least-squares regression.

TABLE I: Power law degree exponent (γ) for FluxANN and CESM2 for different neighborhood structures.

Exponent	FluxANN	CESM2
seld	20.68	6.77
lesd	3.40	2.05
6-n	1.85	1.88
18-n	1.82	1.80
leld	1.83	1.79

where M is the total number of nodes in the network and n_{max}, n_{min} are the degree of largest, smallest node, respectively.

For networks where $1 < \gamma < 2$, the exponent $1/(\gamma - 1)$ would be larger than 1. Therefore, the links or degree of the largest hub grows faster than the size of the network [22]. Hence, a cut-off point that will be reached and the largest hub will not grow any larger. These cut-offs possibly exist in STEs in GPP due to continental discontinuity of terrestrial GPP [11]. The networks with $1 < \gamma < 2$ are categorized as anomalous regimes [22] in which large networks cannot exist.

C. Attribution of Negative STEs in GPP to Climate Drivers

We selected the 100 largest STEs in GPP for attribution to *tas* and *pr* anomalies. We also analyzed the impact of antecedent climatic conditions on negative STEs in GPP and found that as the lagged number of months increases, the number of STEs attributed to a given climatic variable decreases. However, for ease of representing drivers, we reported the average number of STEs driven from a lag of zero to three months. Table II shows the number of negative STEs in GPP using FluxANN driven by various climate drivers from ERA5,
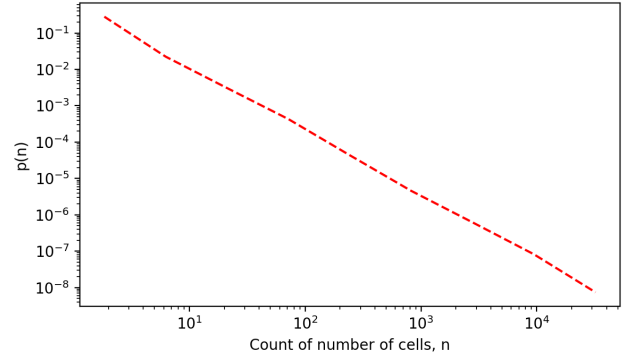
(a) FluxANN
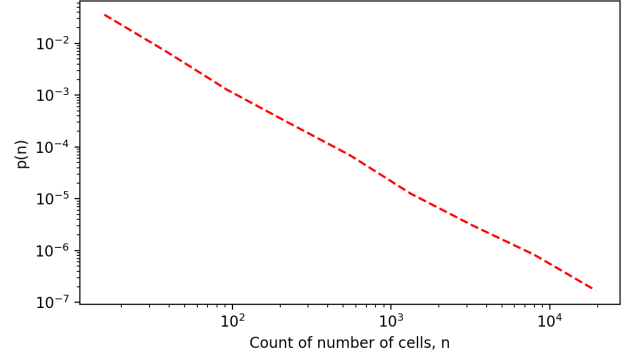
(b) CESM2

Fig. 6: Powerlaw fit for neighborhood structure *leld* for (a) FluxANN and (b) CESM2. The y-axis represents the probability that randomly chosen manifold has n degrees, see equation 5. The x-axis represents the size of the manifold with n nodes. The corresponding power law exponent γ for (a) FluxANN and (b) CESM2 were 1.83 and 1.79, respectively.

and Table III shows attribution of STEs in GPP to climate drivers from CESM2. The dominant climate driver of negative STEs in GPP was the *hot* climatic condition for both FluxANN and CESM2, followed by the *cold* climatic condition. The dominance of *hot* events on negative STEs in GPP was seen for all neighborhood structures. However, the dominance of *hot* events driving negative STEs declined as the number of neighbors in neighborhood structures increased in CESM2; for *leld* the attribution to *hot:cold* was 50:50. The number of STEs driven by *dry* and *wet* were very rare. These attribution results were in contrast to the findings from other studies [1], [7]–[11], which requires further investigation. Main difference between this attribution analysis and prior work was identified that could have driven differences in our results. Recent studies [9], [9] have performed attribution analysis at every grid and a few studies [7], [11] have compared the left and right tails of distribution of climate drivers based of a moving window of STEs in GPP relative to the median of the climate drivers during STEs in GPP. Here, we represented the median climatic condition for the whole manifold of STEs in GPP at antecedent time steps and compare it with a median climatic condition

TABLE II: Attribution of negative carbon cycle STEs from FluxANN to monthly average surface temperature and precipitation from ERA5. The first and fourth quartile values of drivers were used to define cold, hot, dry, and wet climatic conditions. The attribution analysis is conducted for top 100 STEs. The values represent average response of STEs to climate drivers from lag of zero months to three months.

FluxANN	*cold*	*hot*	*dry*	*wet*
seld	3	13	4	1
lesd	4	18	2	1
6-n	1	10	0	0
18-n	2	11	0	0
leld	1	10	0	0

TABLE III: Attribution of negative carbon cycle STEs from FluxANN to monthly average surface temperature and precipitation from ERA5. The first and fourth quartile values of drivers were used to define cold, hot, dry, and wet climatic conditions. The attribution analysis is conducted for top 100 STEs. The values represent average response of STEs to climate drivers from lag of zero months to three months.

CESM2	*cold*	*hot*	*dry*	*wet*
seld	0	38	0	1
lesd	7	19	1	3
6-n	5	9	1	0
18-n	4	7	0	0
leld	5	5	0	1

during a STE event in GPP.

Since the distribution of STEs in GPP follow a power law, the top 100 STEs represent very large extent and long duration events. Our aim was to compute representative climatic condition for each driver during and prior to STEs. One drawback of this approach is that summarizing the climatic conditions to one value per STE cannot represent the regional heterogeneity of climate–carbon cycle feedbacks.

V. CONCLUSIONS

The comparative analysis of carbon cycle STEs among observation (FluxANN) and ESM (CESM2) indicated that:

1) The magnitude of losses in carbon uptake during negative STEs in GPP were larger in CESM2 than FluxANN. One of the main reason of underestimating the magnitude of negative carbon cycle extremes in FluxANN is due to low variability in carbon cycle fluxes.
2) The largest magnitude of negative carbon cycle extremes were in the tropical regions, especially in the Amazon Basin.
3) The area affected and the magnitude of carbon losses during negative STEs in GPP were largely dependent and proportional to the neighborhood structure of STEs.

4) More than 75% of cumulative carbon loss during negative STEs in GPP was represented by less than 100 STEs.
5) The largest driver of negative STEs in GPP was *hot* climatic conditions.
6) As the size of the neighborhood structure increased, the attribution of negative STEs in GPP to *hot*:*cold* reduced. Further analysis is needed to understand these patterns.

Further analysis is needed to investigate the reasons for fewer attribution of negative STEs in GPP to *dry* climatic conditions, which has been found to be the dominant driver of negative carbon cycle extremes in other studies [1], [8], [9]. This study aimed to inform the community that the choice of neighborhood structure to find the spatiotemporal manifold in carbon cycle extremes governs the characteristics of continuous, constrained continuous, and non-continuous extremes that vary largely in magnitude and the area affect by extremes as well as the attribution to climate drivers.

OPEN RESEARCH

The details of the data and its availability is mentioned in the Section II.

This data analysis was performed in Python, and the analysis codes are available on GitHub at https://github.com/sharma-bharat/Codes_SpatioTemporalExtremes.git.

REFERENCES

[1] Reichstein, Markus and Bahn, Michael and Ciais, Philippe and Frank, Dorothea and Mahecha, Miguel D. and Seneviratne, Sonia I. and Zscheischler, Jakob and Beer, Christian and Buchmann, Nina and Frank, David C. and Papale, Dario and Rammig, Anja and Smith, Pete and Thonicke, Kirsten and van der Velde, Marijn and Vicca, Sara and Walz, Ariane and Wattenbach, Martin "Climate extremes and the carbon cycle". Nature, 500(7462), 287–295. https://doi.org/10.1038/nature12350, 2013.

[2] Friedlingstein, P., Jones, M. W., O'Sullivan, M., Andrew, R. M., Bakker, D. C. E., Hauck, J., Le Quéré, C., Peters, G. P., Peters, W., Pongratz, J., Sitch, S., Canadell, J. G., Ciais, P., Jackson, R. B., Alin, S. R., Anthoni, P., Bates, N. R., Becker, M., Bellouin, N., Bopp, L., Chau, T. T. T., Chevallier, F., Chini, L. P., Cronin, M., Currie, K. I., Decharme, B., Djeutchouang, L. M., Dou, X., Evans, W., Feely, R. A., Feng, L., Gasser, T., Gilfillan, D., Gkritzalis, T., Grassi, G., Gregor, L., Gruber, N., Gürses, Ö., Harris, I., Houghton, R. A., Hurtt, G. C., Iida, Y., Ilyina, T., Luijkx, I. T., Jain, A., Jones, S. D., Kato, E., Kennedy, D., Klein Goldewijk, K., Knauer, J., Korsbakken, J. I., Körtzinger, A., Landschützer, P., Lauvset, S. K., Lefèvre, N., Lienert, S., Liu, J., Marland, G., McGuire, P. C., Melton, J. R., Munro, D. R., Nabel, J. E. M. S., Nakaoka, S.-I., Niwa, Y., Ono, T., Pierrot, D., Poulter, B., Rehder, G., Resplandy, L., Robertson, E., Rödenbeck, C., Rosan, T. M., Schwinger, J., Schwingshackl, C., Séférian, R., Sutton, A. J., Sweeney, C., Tanhua, T., Tans, P. P., Tian,

H., Tilbrook, B., Tubiello, F., van der Werf, G. R., Vuichard, N., Wada, C., Wanninkhof, R., Watson, A. J., Willis, D., Wiltshire, A. J., Yuan, W., Yue, C., Yue, X., Zaehle, S., and Zeng, J.: Global Carbon Budget 2021, Earth Syst. Sci. Data, 14, 1917–2005, https://doi.org/10.5194/essd-14-1917-2022, 2022.

[3] Schimel, D., Stephens, B. B., and Fisher, J. B., "Effect of increasing CO_2 on the terrestrial carbon cycle," Proceedings of the National Academy of Sciences, vol. 112, no. 2, pp. 436–441, https://doi.org/10.1073/pnas.1407302112, 2015.

[4] Frank, D., Reichstein, M., Bahn, M., Thonicke, K., Frank, D., Mahecha, M.D., Smith, P., van der Velde, M., Vicca, S., Babst, F., Beer, C., Buchmann, N., Canadell, J.G., Ciais, P., Cramer, W., Ibrom, A., Miglietta, F., Poulter, B., Rammig, A., Seneviratne, S.I., Walz, A., Wattenbach, M., Zavala, M.A. and Zscheischler, J., "Effects of climate extremes on the terrestrial carbon cycle: concepts, processes and potential future impacts," Glob Change Biol, 21: 2861-2880. https://doi.org/10.1111/gcb.12916, 2015.

[5] Flach, M., Brenning, A., Gans, F., Reichstein, M., Sippel, S., and Mahecha, M. D., "Vegetation modulates the impact of climate extremes on gross primary production," Biogeosciences Discussions, 2020, 1–20, https://doi.org/10.5194/bg-2020-80, 2020.

[6] Piao, S., Sitch, S., Ciais, P., Friedlingstein, P., Peylin, P., Wang, X., Ahlström, A., Anav, A., Canadell, J.G., Cong, N., Huntingford, C., Jung, M., Levis, S., Levy, P.E., Li, J., Lin, X., Lomas, M.R., Lu, M., Luo, Y., Ma, Y., Myneni, R.B., Poulter, B., Sun, Z., Wang, T., Viovy, N., Zaehle, S. and Zeng, N., "Evaluation of terrestrial carbon cycle models for their response to climate variability and to CO_2 trends," Global Change Biology, 19: 2117-2132. https://doi.org/10.1111/gcb.12187, 2013.

[7] Zscheischler, J., Reichstein, M., Buttlar, J. von, Mu, M., Randerson, J. T., and Mahecha, M. D., "Carbon cycle extremes during the 21st century in CMIP5 models: Future evolution and attribution to climatic drivers," Geophys. Res. Lett., 41, 8853–8861, doi:10.1002/2014GL062409, 2014.

[8] Sharma, B., Kumar, J., Ganguly, A. R., and Hoffman, F. M., "Carbon Cycle Extremes Accelerate Weakening of the Land Carbon Sink in the Late 21st Century," Biogeosciences Discuss. [preprint], https://doi.org/10.5194/bg-2022-178, in review, 2022.

[9] Sharma, B., Kumar, J., Collier, N., Ganguly, A. R., & Hoffman, F. M., "Quantifying carbon cycle extremes and attributing their causes under climate and land use and land cover change from 1850 to 2300," Journal of Geophysical Research: Biogeosciences, 127, e2021JG006738. https://doi.org/10.1029/2021JG006738, 2022.

[10] Zscheischler, J., Mahecha, M. D., von Buttlar, J., Harmeling, S., Jung, M., Rammig, A., Randerson, J. T., Schölkopf, B., Seneviratne, S. I., Tomelleri, E., Zaehle, S., and Reichstein, M., "A few extreme events dominate global interannual variability in gross primary production," Environmental Research Letters, 9, 035 001, https://doi.org/10.1088/1748-9326/9/3/035001, 2014.

[11] Zscheischler, J., Mahecha, M. D., Harmeling, S., and Reichstein, M., "Detection and attribution of large spatiotemporal extreme events in Earth observation data," Ecological Informatics, Volume 15, 2013, Pages 66–73, ISSN 1574–9541, https://doi.org/10.1016/j.ecoinf.2013.03.004.

[12] Jung, M. and Schwalm, C. and Migliavacca, M. and Walther, S. and Camps-Valls, G. and Koirala, S. and Anthoni, P. and Besnard, S. and Bodesheim, P. and Carvalhais, N. and Chevallier, F. and Gans, F. and Goll, D. S. and Haverd, V. and Köhler, P. and Ichii, K. and Jain, A. K. and Liu, J. and Lombardozzi, D. and Nabel, J. E. M. S. and Nelson, J. A. and O'Sullivan, M. and Pallandt, M. and Papale, D. and Peters, W. and Pongratz, J. and Rödenbeck, C. and Sitch, S. and Tramontana, G. and Walker, A. and Weber, U. and Reichstein, M., "Scaling carbon fluxes from eddy covariance sites to globe: synthesis and evaluation of the FLUXCOM approach," Biogeosciences, vol. 17, no. 5, pp. 1343–1365, https://doi.org/10.5194/bg-17-1343-2020, 2020.

[13] X. Li and J. Xiao, "A global, 0.05-degree product of solar-induced chlorophyll fluorescence derived from OCO-2, MODIS, and reanalysis data," Remote Sensing, vol. 11, no. 5, https://doi.org/10.3390/rs11050517, 2019.

[14] Ullrich, Paul A. and Taylor Mark A., "Arbitrary-Order Conservative and Consistent Remapping and a Theory of Linear Maps: Part 1." Mon. Weather Rev., 143, 2419–2440, https://10.1175/MWR-D-14-00343.1, 2015

[15] Ullrich, Paul A., Devendran, Darshi, and Johansen, Hans, "Arbitrary-Order Conservative and Consistent Remapping and a Theory of Linear Maps, Part 2." Mon. Weather Rev., 144, 1529–1549, https://10.1175/MWR-D-15-0301.1, 2016

[16] Golyandina, N., Nekrutkin, V. and Zhigljavsky, A. A., "Analysis of Time Series Structure: SSA and Related Techniques," 1st ed. Chapman and Hall/CRC, Jan. 2001.

[17] Seneviratne, S. I., Nicholls, N., Easterling, D., Goodess, C. M., Kanae, S., Kossin, J., Luo, Y., Marengo, J., McInnes, K., Rahimi, M., Reichstein, M., Sorteberg, A., Vera, C., and Zhang, X.: Changes in Climate Extremes and their Impacts on the Natural Physical Environment, pp. 109–230, Cambridge Univ. Press, Cambridge, U.K., and New York, [Field, C.B., V. Barros, T.F. Stocker, D. Qin, D.J. Dokken, K.L. Ebi, M.D. Mastrandrea, K.J. Mach, G.-K. Plattner, S.K. Allen, M. Tignor, and P.M. Midgley (eds.)]. A Special Report of Working Groups I and II of the Intergovernmental Panel on Climate Change (IPCC), 2012.

[18] Zhang, T., Xu, M., Xi, Y., Zhu, J., Tian, L., Zhang, X., Wang, Y., Li, Y., Shi, P., Yu, G., Sun, X., and Zhang, Y., "Lagged climatic effects on carbon fluxes over three grassland ecosystems in China, Journal of Plant Ecology," 8, 291–302, https://doi.org/10.1093/jpe/rtu026, 2014.

[19] Williams, I. N., Torn, M. S., Riley, W. J., & Wehner, M. F, "Impacts of climate extremes on gross primary production under global warming," Environmental Research Letters, 9(9), 094011, https://doi.org/10.1088/1748-9326/9/9/094011, 2014

[20] Piao, Shilong and Zhang, Xinping and Chen, Anping and Liu, Qiang and Lian, Xu and Wang, Xuhui and Peng, Shushi and Wu, Xiuchen "The impacts of climate extremes on the terrestrial carbon cycle: A review," Sci. China Earth Sci. 62, 1551–1563, https://doi.org/10.1007/s11430-018-9363-5, 2019.

[21] Copernicus Climate Change Service (C3S), "ERA5: Fifth generation of ecmwf atmospheric reanalyses of the global climate," Copernicus Climate Change Service Climate Data Store (CDS), vol. 15, no. 2, p. 2020, 2017.

[22] Barabási Albert-László, "Network science," Phil. Trans. R. Soc. A371:20120375 http://doi.org/10.1098/rsta.2012.0375, 2013.

[23] Warner, M., Sharma, B., Bhatia, U., and Ganguly, A., "Evaluation of Cascading Infrastructure Failures and Optimal Recovery from a Network Science Perspective.", In: Ghanbarnejad, F., Saha Roy, R., Karimi, F., Delvenne, JC., Mitra, B. (eds) Dynamics On and Of Complex Networks III. DOOCN 2017. Springer Proceedings in Complexity. Springer, Cham. https://doi.org/10.1007/978-3-030-14683-2_3